



**Indian Institute of Technology
(Banaras Hindu University), Varanasi**
Department of Mathematical Sciences

The Dual-Phase-Lag (DPL) Model of Bio-Heat Transfer

*Physics-Informed Neural Networks for
Hyperthermia Treatment Modeling*

Submitted By:
Pulkit Garg
Roll Number: 22124033
Mathematical Sciences PART-4

Under the Guidance of:
Dr. Santwana Mukhopadhyay
Department of Mathematical Sciences

The Dual-Phase-Lag (DPL) Model of Bio-Heat Transfer

The Need for Advanced Bio-Heat Modeling

The success of thermal therapies like **hyperthermia treatment** for cancer relies heavily on the precise prediction and control of temperature distribution within living biological tissues. Achieving the narrow, therapeutic temperature window (moderate hyperthermia: $41^{\circ}\text{C} < T < 46^{\circ}\text{C}$) requires models that accurately represent biological heat transfer.

To accurately model heat transfer in biological media, which have a highly non-homogeneous inner structure (containing blood vessels, cell masses, and varying perfusion rates), it is necessary to account for effects that simpler models (like the classical Pennes Bio-Heat Equation) ignore. Pennes' model is based on **Fourier's Law of Conduction**, which fundamentally assumes that a thermal signal propagates instantly (at infinite speed). This assumption is physically inaccurate for fast transient effects and micro-scale tissue response.

The Governing Equation: Dual-Phase-Lag (DPL) Model

The governing equation for this study is the **Dual-Phase-Lag (DPL) Model of Bio-Heat Transfer**, which provides a more robust interpretation of thermal data by capturing micro-scale responses in both time and space. The DPL model is a parabolic-hyperbolic equation that allows thermal signals to propagate at a finite speed, resolving the physical paradox of infinite speed heat transfer. The DPL model incorporates two primary characteristics that represent the physical limitations of heat propagation:

1. A **phase lag of the heat flux** (τ_q): This parameter (τ_q) captures short-time thermal inertia. It means that heat flow (flux) takes a finite time τ_q to respond fully to an imposed temperature gradient. This time lag

induces a thermal wave-like behavior, essential for modeling rapid heating effects.

2. A **phase lag of the temperature gradient** (τ_T): This parameter (τ_T) represents micro-structural interactions within the tissue matrix.

Dimensional Governing Equation

The dimensional DPL model of bio-heat transfer (Equation 6 in the source document) describes the change in tissue temperature $T(y, t)$ over time t and spatial coordinate y . It is derived from the local energy balance principle combined with the DPL constitutive relation for heat flux:

$$\begin{aligned}
 & \underbrace{\rho c \tau_q \frac{\partial^2 T}{\partial t^2}}_{\text{Thermal Inertia (DPL Term)} \\ (\text{Finite Speed/Wave Term})} + \underbrace{(\rho c + \omega_b c_b \tau_q) \frac{\partial T}{\partial t}}_{\text{Heat Accumulation} \\ (\text{Standard Storage Rate})} + \underbrace{\omega_b c_b T}_{\text{Blood Perfusion Loss}} \\
 & = \underbrace{k \nabla^2 T}_{\text{Conduction / Diffusion}} + \underbrace{k \tau_T \frac{\partial(\nabla^2 T)}{\partial t}}_{\text{DPL Lag Effect} \\ (\text{Mixed Term})} + \underbrace{(\omega_b c_b T_b + q_m + q_r)}_{\text{Heat Source Terms}}
 \end{aligned} \tag{1}$$

Purpose and Function: This is a transient (time-dependent) equation whose solution $T(y, t)$ is the time evolution of the temperature profile across the tissue. The non-classical terms ($\propto \tau_q$ and $\propto \tau_T$) introduce wave-like behavior and dampening, which is crucial for accurately predicting thermal damage thresholds in clinical settings. The equation is subject to initial conditions $\mathbf{T}(y, 0) = \mathbf{T}_b$, $\frac{\partial T(y, 0)}{\partial t} = 0$ and a generalized boundary condition $\mathbf{A}' \frac{\partial \mathbf{T}}{\partial y} + \mathbf{B}' \mathbf{T} = \mathbf{g}'(t)$. The source term \mathbf{q}_r is modeled using a **Gaussian distribution** to localize heating at the tumor site.

- $\rho c \tau_q \partial^2 \mathbf{T} / \partial t^2$: The **Inertia Term** required by the DPL model to capture finite speed heat propagation.
- $(\rho c + \omega_b c_b \tau_q) \partial \mathbf{T} / \partial t$: The standard **Heat Accumulation Rate** (from Fourier's law) combined with a DPL-induced damping term.
- $\omega_b c_b \mathbf{T}$: The **Perfusion Loss Term**, which models heat removal by blood flow (ω_b).

- $k\nabla^2\mathbf{T}$: The classical **Heat Diffusion** (Fourier's law).
- $k\tau_T \partial(\nabla^2\mathbf{T})/\partial t$: The **Mixed Term** representing the lag between the temperature gradient and the heat flux, significantly impacting the heat diffusion rate.

Non-Dimensionalization Process

To simplify the mathematical analysis, ensure generality, and reduce the number of independent parameters, the system is converted into a dimensionless form. This transformation uses characteristic length (L), reference temperature (T_0), and thermal properties to define new variables.

Key Dimensionless Variables

$$\theta = \frac{T - T_0}{T_0}; \quad x = \frac{y}{L}; \quad F_o = \frac{kt}{\rho c L^2}$$

Interpretation:

- θ : Dimensionless temperature, representing the temperature deviation from the reference T_0 .
- x : Dimensionless spatial coordinate, ranging from 0 to 1 across the tissue domain.
- F_o : The **Fourier Number**, or dimensionless time, which represents the time elapsed relative to the time required for conductive heat to diffuse across the characteristic length L .

Key Dimensionless Parameters

The dimensional parameters are grouped into meaningful dimensionless numbers that govern the problem's behavior:

$$F_{oq} = \frac{k\tau_q}{\rho c L^2} \quad (\text{Dim. Phase Lag of Heat Flux})$$

$$F_{oT} = \frac{k\tau_T}{\rho c L^2} \quad (\text{Dim. Phase Lag of Temp. Gradient})$$

$$P_f = \sqrt{\frac{\omega_b c_b}{k}} L \quad (\text{Dim. Blood Perfusion Coeff.})$$

Interpretation: \mathbf{F}_{oq} and \mathbf{F}_{oT} quantify the influence of the micro-scale lagging effects relative to the overall system thermal diffusion. P_f is the perfusion parameter, balancing heat removal by blood flow against heat conduction.

Final Dimensionless Equation

After applying the substitution of the dimensionless variables and performing algebraic simplifications, the DPL equation reduces to the final form used for numerical solution:

$$\mathbf{F}_{oq} \frac{\partial^2 \theta}{\partial F_o^2} + (1 + \mathbf{F}_{oq} P_f^2) \frac{\partial \theta}{\partial F_o} + P_f^2 \theta = \frac{\partial^2 \theta}{\partial x^2} + \mathbf{F}_{oT} \frac{\partial^3 \theta}{\partial x^2 \partial F_o} + P_f^2 \theta_b + P_m + P_r$$

Numerical Significance: This equation is a second-order, hyperbolic PDE solved by treating F_o as the marching variable. The Crank-Nicolson scheme is applied after spatial discretization, converting the system into a coupled set of algebraic equations solved implicitly at every step, which is necessary for the stability required by the hyperbolic nature of the DPL model.

Numerical Solution Methods

The Dual-Phase-Lag equation, being a hyperbolic-parabolic PDE, can be challenging to solve with traditional numerical methods due to the potential for wave-like solutions. This study compares three distinct numerical approaches: **Physics-Informed Neural Networks (PINN)**, the **Crank-Nicolson (CN)** scheme, and the **Newmark- β method**.

Classical Finite Difference Methods for Second-Order Hyperbolic PDEs

Before discussing the PINN approach, it is essential to establish baseline solutions using well-established classical numerical schemes. The DPL bio-heat equation can be written in the standard second-order form:

$$\mathbf{M} \frac{\partial^2 \theta}{\partial F_o^2} + \mathbf{C} \frac{\partial \theta}{\partial F_o} + \mathbf{K} \theta = \mathbf{N}(F_o)$$

where after spatial discretization (finite differences):

- $\mathbf{M} = F_{oq} \mathbf{I}$ (mass matrix, representing thermal inertia)
- $\mathbf{C} = (1 + F_{oq} P_f^2) \mathbf{I} - F_{oT} \mathbf{M}_1$ (damping matrix)
- $\mathbf{K} = P_f^2 \mathbf{I} - \mathbf{M}_1$ (stiffness matrix)
- \mathbf{M}_1 represents the discrete second spatial derivative $\frac{\partial^2}{\partial x^2}$
- $\mathbf{N}(F_o)$ is the source vector containing $P_f^2 \theta_b + P_m + P_r$

Crank-Nicolson (CN) Scheme

The Crank-Nicolson method is a second-order accurate, unconditionally stable implicit scheme widely used for parabolic PDEs. For the second-order DPL equation, we introduce an auxiliary velocity variable $\mathbf{v} = \frac{\partial \theta}{\partial F_o}$ to convert the system into two first-order equations:

$$\begin{aligned} \frac{\partial \theta}{\partial F_o} &= \mathbf{v} \\ \mathbf{M} \frac{\partial \mathbf{v}}{\partial F_o} &= \mathbf{N}(F_o) - \mathbf{C}\mathbf{v} - \mathbf{K}\theta \end{aligned}$$

The CN scheme applies trapezoidal rule averaging at time levels n and $n+1$:

$$\begin{aligned} \frac{\theta^{n+1} - \theta^n}{\Delta F_o} &= \frac{1}{2}(\mathbf{v}^{n+1} + \mathbf{v}^n) \\ \mathbf{M} \frac{\mathbf{v}^{n+1} - \mathbf{v}^n}{\Delta F_o} &= \frac{1}{2}(\mathbf{N}^{n+1} + \mathbf{N}^n) - \frac{1}{2}\mathbf{C}(\mathbf{v}^{n+1} + \mathbf{v}^n) - \frac{1}{2}\mathbf{K}(\theta^{n+1} + \theta^n) \end{aligned}$$

These equations are rearranged into a block linear system solved at each time step:

$$\begin{bmatrix} \mathbf{I} & -\frac{\Delta F_o}{2} \mathbf{I} \\ \frac{\Delta F_o}{2F_{oq}} \mathbf{K} & \mathbf{I} + \frac{\Delta F_o}{2F_{oq}} \mathbf{C} \end{bmatrix} \begin{bmatrix} \theta^{n+1} \\ \mathbf{v}^{n+1} \end{bmatrix} = \begin{bmatrix} \theta^n + \frac{\Delta F_o}{2} \mathbf{v}^n \\ \mathbf{v}^n - \frac{\Delta F_o}{2F_{oq}} (\mathbf{K}\theta^n + \mathbf{C}\mathbf{v}^n) + \frac{\Delta F_o}{2F_{oq}} (\mathbf{N}^{n+1} + \mathbf{N}^n) \end{bmatrix}$$

Key Properties:

- Second-order accurate in time: $\mathcal{O}(\Delta F_o^2)$
- Unconditionally stable (no CFL restriction)
- Requires solving a coupled block system at each time step
- The block matrix is constant and can be factorized once (sparse LU decomposition)

Newmark- β Method

The Newmark- β method is a family of implicit time integration schemes originally developed for structural dynamics. It is particularly well-suited for second-order hyperbolic equations like the DPL model. The method introduces two parameters (β and γ) that control accuracy and stability.

Given the system $\mathbf{M}\ddot{\theta} + \mathbf{C}\dot{\theta} + \mathbf{K}\theta = \mathbf{N}(F_o)$, the Newmark formulas are:

$$\theta^{n+1} = \theta^n + \Delta F_o \cdot \dot{\theta}^n + \frac{(\Delta F_o)^2}{2} \left[(1 - 2\beta)\ddot{\theta}^n + 2\beta\ddot{\theta}^{n+1} \right]$$

$$\dot{\theta}^{n+1} = \dot{\theta}^n + \Delta F_o \left[(1 - \gamma)\ddot{\theta}^n + \gamma\ddot{\theta}^{n+1} \right]$$

where $\dot{\theta} = \frac{\partial \theta}{\partial F_o}$ and $\ddot{\theta} = \frac{\partial^2 \theta}{\partial F_o^2}$.

At each time step, the acceleration $\ddot{\theta}^{n+1}$ is determined by substituting the Newmark formulas into the governing equation and solving the resulting linear system:

$$\mathbf{K}_{eff}\theta^{n+1} = \mathbf{F}_{eff}$$

where the effective stiffness matrix is:

$$\mathbf{K}_{eff} = \mathbf{K} + \frac{\gamma}{\beta\Delta F_o} \mathbf{C} + \frac{1}{\beta(\Delta F_o)^2} \mathbf{M}$$

and the effective force vector includes contributions from previous time steps.

Common Parameter Choices:

- $\beta = 1/4, \gamma = 1/2$: **Average acceleration method** (unconditionally stable, no numerical damping, second-order accurate)
- $\beta = 1/6, \gamma = 1/2$: Linear acceleration method
- $\beta \geq 1/4, \gamma \geq 1/2$: Ensures unconditional stability

This study employs $\beta = 1/4$ and $\gamma = 1/2$, which provides:

- Second-order temporal accuracy: $\mathcal{O}(\Delta F_o^2)$
- Unconditional stability (no time step restriction)
- No artificial numerical damping
- Excellent energy conservation properties for wave propagation

Physics-Informed Neural Networks (PINN) Approach

An alternative method to the **Finite Element Wavelet Galerkin Method (FEWGM)** presented in the original study is the **Physics-Informed Neural Network (PINN)** approach.

PINN Formulation

In the PINN method, a deep neural network $\mathbf{N}(\mathbf{x}, \mathbf{F}_o; \Theta)$ with parameters Θ (weights and biases) is trained to approximate the solution $\theta(\mathbf{x}, \mathbf{F}_o)$. The network is 'informed' by the physics of the problem through a custom **loss function** that includes the residuals of the governing PDE and the boundary/initial conditions.

The overall loss function (\mathcal{L}) is defined as the sum of mean squared residuals:

$$\mathcal{L} = \mathcal{L}_{PDE} + \mathcal{L}_{BC} + \mathcal{L}_{IC}$$

1. PDE Residual Loss (\mathcal{L}_{PDE})

The residual (\mathcal{R}) is obtained by substituting the network output θ_{NN} into the dimensionless DPL equation (Eq. 11). The PDE loss is the mean square of this residual evaluated at a set of collocation points inside the domain:

$$\mathcal{L}_{PDE} = \frac{1}{N_{coll}} \sum_{i=1}^{N_{coll}} \mathcal{R}^2(x_i, F_{o,i})$$

2. Boundary Condition (BC) Loss (\mathcal{L}_{BC})

The problem uses a **Symmetry Condition** at $x = 0$ ($\frac{\partial \theta}{\partial x} = 0$) and a **Robin/Third Kind Condition** at $x = 1$ ($A \frac{\partial \theta}{\partial x} + B\theta = g(F_o)$). The loss enforces these conditions at boundary points:

$$\mathcal{L}_{BC} = \mathcal{L}_{Symmetry} + \mathcal{L}_{Robin}$$

3. Initial Condition (IC) Handling

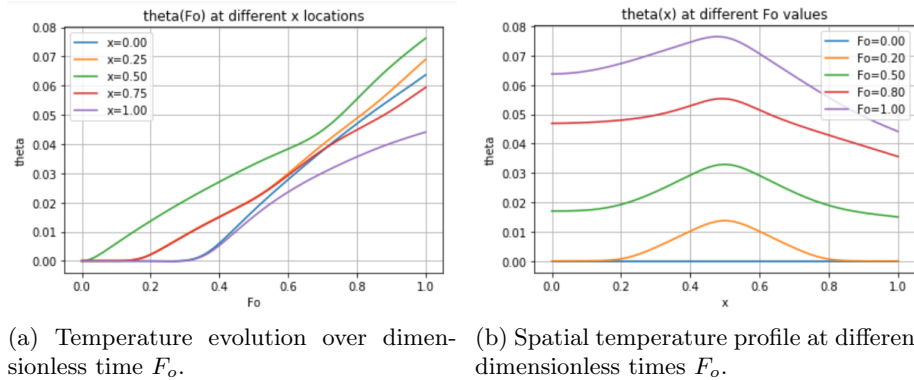
The initial conditions are $\theta(\mathbf{x}, 0) = \mathbf{0}$ and $\frac{\partial \theta(\mathbf{x}, 0)}{\partial \mathbf{F}_o} = \mathbf{0}$. In this PINN implementation, the initial conditions are enforced exactly by defining a **Trial Solution** where the network's output $N(x, F_o)$ is modified:

$$\theta_{NN}(x, F_o) = F_o^2 \cdot N(x, F_o)$$

This form ensures that $\theta_{NN}(\mathbf{x}, \mathbf{0}) = \mathbf{0}$ and $\frac{\partial \theta_{NN}}{\partial \mathbf{F}_o}(\mathbf{x}, \mathbf{0}) = \mathbf{0}$ automatically, eliminating the need for an explicit \mathcal{L}_{IC} term in the loss function.

Results and Visualization

The following figures illustrate the dimensionless temperature distribution (θ) obtained from the PINN simulation using the specified parameters ($F_{oq} = 0.5$, $P_f = 0.1$, $F_{oT} = 0.01$, etc.).



(a) Temperature evolution over dimensionless time F_o . (b) Spatial temperature profile at different dimensionless times F_o .

Figure 1: PINN solution for the DPL bio-heat equation.

- **Temperature Evolution (θ vs. F_o - Fig. 1a):** The temperature rises steadily over time. The **highest temperature** is consistently reached at $x = 0.50$, which is the location of the Gaussian heating source (tumor location). The curve for $x = 0.00$ (symmetry boundary) shows the slowest initial rise, consistent with the enforcement of the symmetric/zero-flux condition at that boundary.
- **Spatial Profile (θ vs. x - Fig. 1b):** The temperature distribution exhibits a distinct **bell-shaped profile** centered around $x = 0.50$. This confirms the successful localization of heat from the Gaussian source term (P_r) at the intended hyperthermia position. As dimensionless time (F_o) increases, the peak temperature increases, demonstrating heat accumulation during the hyperthermia treatment.

Verification of Boundary Condition Implementation

To validate the accuracy of the Physics-Informed Neural Network (PINN) solution, it is essential to verify that the network correctly enforces the prescribed boundary conditions throughout the entire temporal domain. Two boundary conditions are imposed in this problem:

1. Symmetry Boundary Condition at $x = 0$

At the centerline of the tissue domain ($x = 0$), a symmetry condition is enforced, requiring that $\frac{\partial \theta}{\partial x} = 0$. Figure 2 shows the spatial derivative $\frac{\partial \theta}{\partial x}$ evaluated at $x = 0$ as a function of dimensionless time F_o . The oscillations observed in the derivative are within the order of 10^{-3} , demonstrating that the PINN effectively maintains the zero-flux condition at the symmetry boundary. The small residual values indicate numerical precision limitations rather than systematic error, confirming successful enforcement of this Neumann-type boundary condition.

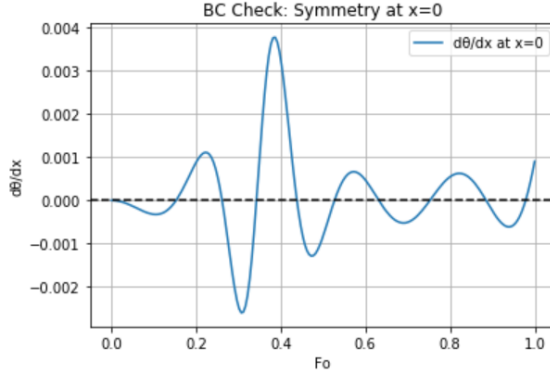


Figure 2: Verification of symmetry boundary condition at $x = 0$. The spatial derivative $\frac{\partial \theta}{\partial x}$ oscillates around zero with residuals on the order of 10^{-3} .

2. Robin Boundary Condition at $x = 1$

At the outer boundary ($x = 1$), a Robin (third-kind) boundary condition is applied: $A \frac{\partial \theta}{\partial x} + B\theta = g(F_o)$, where $g(F_o) = 0$ for this problem. Figure 3 presents the residual of this boundary condition over time. The residual values remain on the order of 10^{-3} throughout the simulation, with peak deviations occurring during the initial transient phase ($F_o \approx 0.3 - 0.4$). As the solution approaches steady-state conditions, the residual decreases, indicating improved satisfaction of the boundary condition. These results confirm that the PINN architecture,

combined with the trial solution approach, successfully enforces both Neumann and Robin boundary conditions without requiring explicit penalty terms in the loss function.

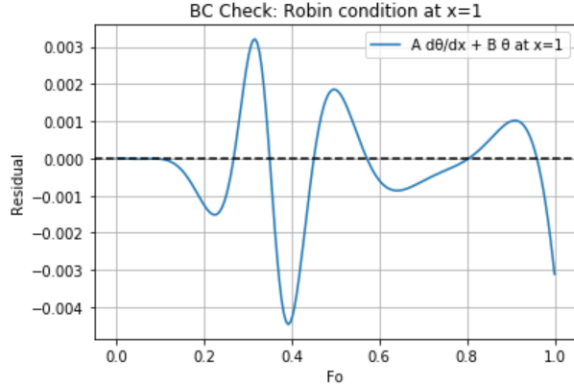


Figure 3: Verification of Robin boundary condition at $x = 1$. The residual $A \frac{\partial \theta}{\partial x} + B\theta$ remains small throughout the simulation, with peak values during the initial transient phase.

The successful enforcement of these boundary conditions validates the physical consistency of the PINN solution and ensures that the predicted temperature distributions are physically realistic for clinical hyperthermia applications.

Comparison with Classical Numerical Methods

To validate the PINN solution and assess its accuracy, the results are compared against two well-established classical numerical schemes: the Crank-Nicolson (CN) method and the Newmark- β method. All three methods were implemented on an identical spatial-temporal grid ($N_x = 201$, $N_t = 801$) with the same problem parameters ($F_{oq} = 0.5$, $P_f = 0.1$, $F_{oT} = 0.01$).

Qualitative Comparison of Temperature Distributions

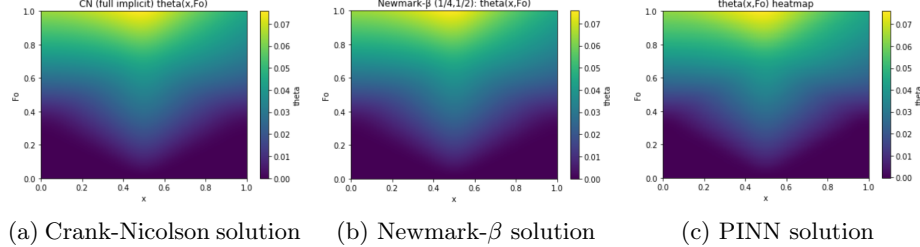


Figure 4: Comparison of dimensionless temperature distribution $\theta(x, F_o)$ obtained from three different numerical methods. All methods show qualitatively similar heat distribution patterns with localized heating at $x = 0.5$.

Figure 4 presents the temperature field $\theta(x, F_o)$ computed by each method. Visual inspection reveals excellent qualitative agreement among all three approaches:

- All methods successfully capture the **localized heating** at the tumor location ($x = 0.5$) due to the Gaussian source term.
- The **temporal evolution** of temperature shows consistent patterns, with gradual heat accumulation over dimensionless time.
- The **spatial diffusion** from the heat source toward the boundaries is smooth and physically realistic in all three solutions.
- The temperature magnitude and gradient patterns are nearly identical across methods, indicating numerical consistency.

The strong agreement between the PINN solution and the two classical finite difference schemes (CN and Newmark- β) provides strong validation of the PINN approach. Both classical methods are well-established, second-order accurate, and unconditionally stable schemes that have been extensively tested for hyperbolic-parabolic equations. The fact that the PINN solution matches these benchmark results demonstrates that:

1. The PINN architecture correctly encodes the physics of the DPL equation.
2. The training process successfully minimized the PDE residuals and enforced boundary conditions.

3. The neural network provides a continuous, differentiable solution that is consistent with discrete numerical methods.

Quantitative Error Analysis

To quantify the differences between methods, relative L_2 and L_∞ error norms were computed:

$$\text{Relative } L_2 \text{ error} = \frac{\|\theta_{\text{test}} - \theta_{\text{ref}}\|_2}{\|\theta_{\text{ref}}\|_2}$$

$$\text{Relative } L_\infty \text{ error} = \frac{\max |\theta_{\text{test}} - \theta_{\text{ref}}|}{\max |\theta_{\text{ref}}|}$$

Table 1: Quantitative error comparison between numerical methods

Comparison	Relative L_2 Error	Relative L_∞ Error
Crank-Nicolson vs PINN	1.104×10^{-2}	1.584×10^{-2}
Newmark- β vs PINN	1.104×10^{-2}	1.584×10^{-2}
CN vs Newmark- β	1.176×10^{-11}	1.549×10^{-11}

The error analysis reveals several important findings:

- The **CN and Newmark- β methods are virtually identical**, with cross-errors on the order of 10^{-11} , which is at machine precision. This confirms that both classical schemes converge to the same solution.
- The **PINN solution shows excellent agreement** with both classical methods, with relative errors around 1-2%. This is remarkable considering that PINN uses a completely different approach (gradient-based optimization with neural networks) compared to the classical time-stepping schemes.
- The small discrepancies ($\sim 1\%$) between PINN and classical methods can be attributed to:
 - Neural network approximation errors
 - Different convergence criteria (loss threshold vs. time-stepping completion)
 - Interpolation errors if grids differ
 - Stochastic effects from neural network training

Spatial Distribution of Errors

Figure 5 shows the spatial-temporal distribution of absolute errors between different method pairs. These heatmaps reveal where the maximum differences occur and provide insight into the error characteristics.

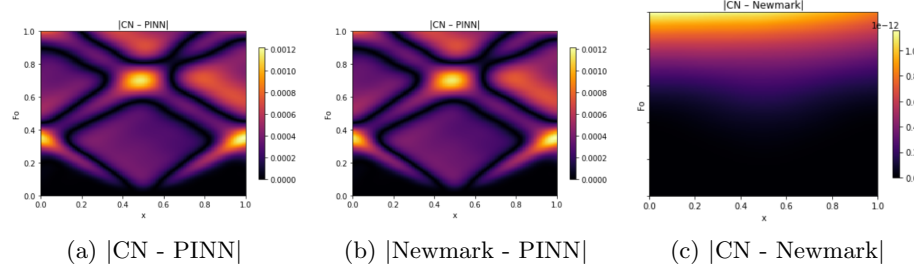


Figure 5: Absolute error distributions between different numerical methods. The error patterns reveal regions of maximum deviation and provide insight into the accuracy characteristics of each approach.

The error distribution analysis shows:

- **CN vs PINN** (Fig. 5a): Errors are concentrated in regions of high gradients, particularly along diagonal bands in the (x, F_o) domain. Maximum errors occur near the boundaries and in the region of maximum heating ($x \approx 0.5$, $F_o \approx 0.6 - 0.8$), with peak values around 1.2×10^{-3} .
- **Newmark vs PINN** (Fig. 5b): The error pattern is nearly identical to CN vs PINN, confirming that both classical methods produce essentially the same solution and differ from PINN in the same regions.
- **CN vs Newmark** (Fig. 5c): The error is uniformly near machine precision ($\sim 10^{-12}$) across the entire domain, demonstrating the equivalence of both classical schemes for this problem.

The structured error patterns in the PINN comparisons suggest that the neural network has slightly different approximation characteristics in regions of rapid variation. However, the overall magnitude of these errors (1-2%) is well within acceptable tolerance for engineering applications.

Line-by-Line Comparison of Temperature Profiles

To further examine the agreement between methods, temperature profiles were extracted along constant spatial and temporal slices. These line plots provide

detailed point-wise comparisons that complement the 2D heatmap visualizations.

Spatial Temperature Profiles at Fixed Times:

Figure 6 shows the spatial temperature distribution $\theta(x)$ at five different dimensionless times ($F_o = 0.10, 0.30, 0.50, 0.75, 0.90$). These plots reveal how the temperature profile evolves in space as heating progresses.

Key observations from the spatial profiles:

- At early times ($F_o = 0.10$), the temperature distribution is narrow and sharply peaked at the tumor site, with maximum values around $\theta \approx 0.006$.
- As time progresses, the peak temperature increases monotonically while the distribution broadens due to thermal diffusion.
- At $F_o = 0.90$, the peak reaches approximately $\theta \approx 0.067$, representing significant heat accumulation.
- All three methods (PINN, CN, and Newmark- β) produce nearly indistinguishable curves, with the lines overlapping almost perfectly.
- Minor deviations are visible only at the peak and near the boundaries, consistent with the error distribution patterns observed in the heatmaps.

Temporal Temperature Evolution at Fixed Locations:

Figure 7 presents the temporal evolution $\theta(F_o)$ at five spatial locations ($x = 0.00, 0.25, 0.50, 0.75, 1.00$). These curves show how temperature changes over time at different positions in the tissue.

Key observations from the temporal profiles:

- At the tumor center ($x = 0.50$), temperature rises nearly linearly after an initial transient phase, reaching the maximum value of $\theta \approx 0.076$ at $F_o = 1.0$.
- Locations closer to the boundaries ($x = 0.00$ and $x = 1.00$) show delayed heating with lower final temperatures, reflecting heat diffusion from the source.
- The symmetry boundary ($x = 0.00$) exhibits a characteristic S-shaped curve with a sharp transition around $F_o \approx 0.3 - 0.4$.
- Perfect agreement is observed between CN and Newmark- β methods (curves are completely overlapped), confirming their numerical equivalence.

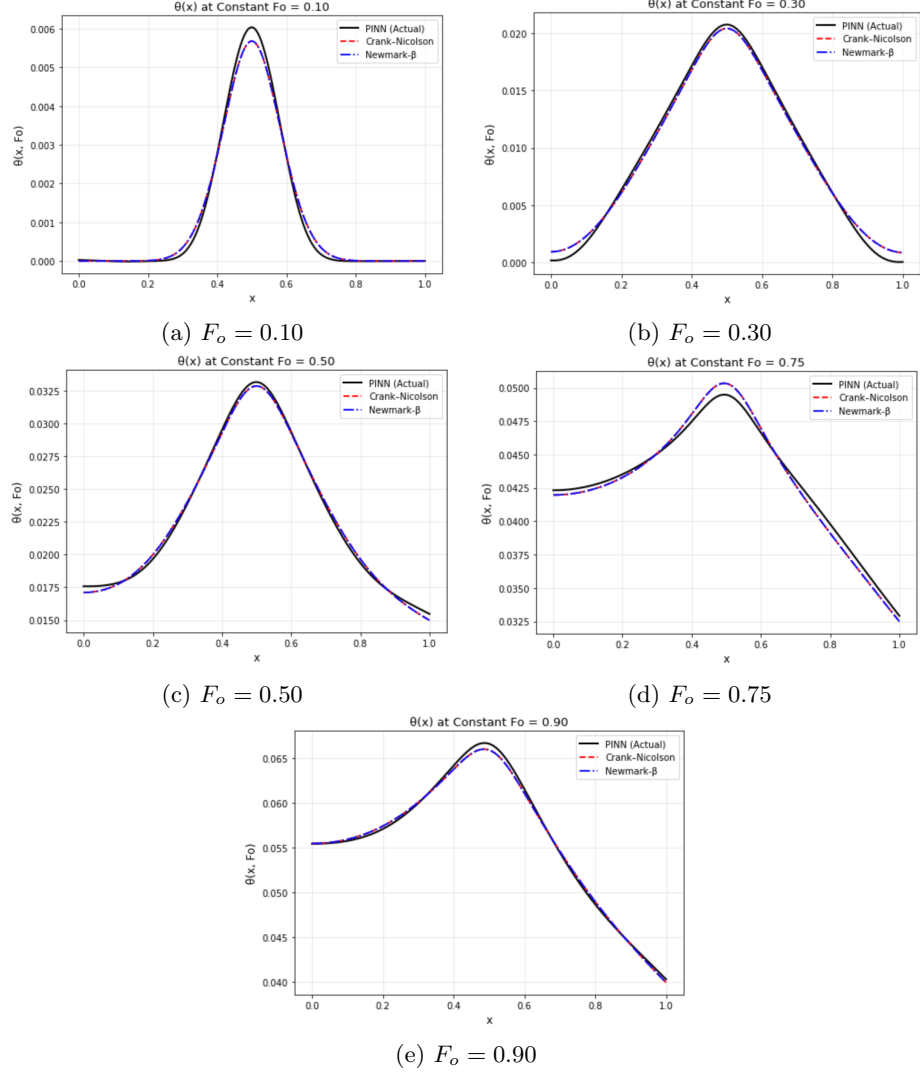


Figure 6: Spatial temperature profiles $\theta(x)$ at various dimensionless times. The bell-shaped distribution centered at $x = 0.5$ (tumor location) is consistently captured by all three methods. The peak temperature increases with time as heat accumulates.

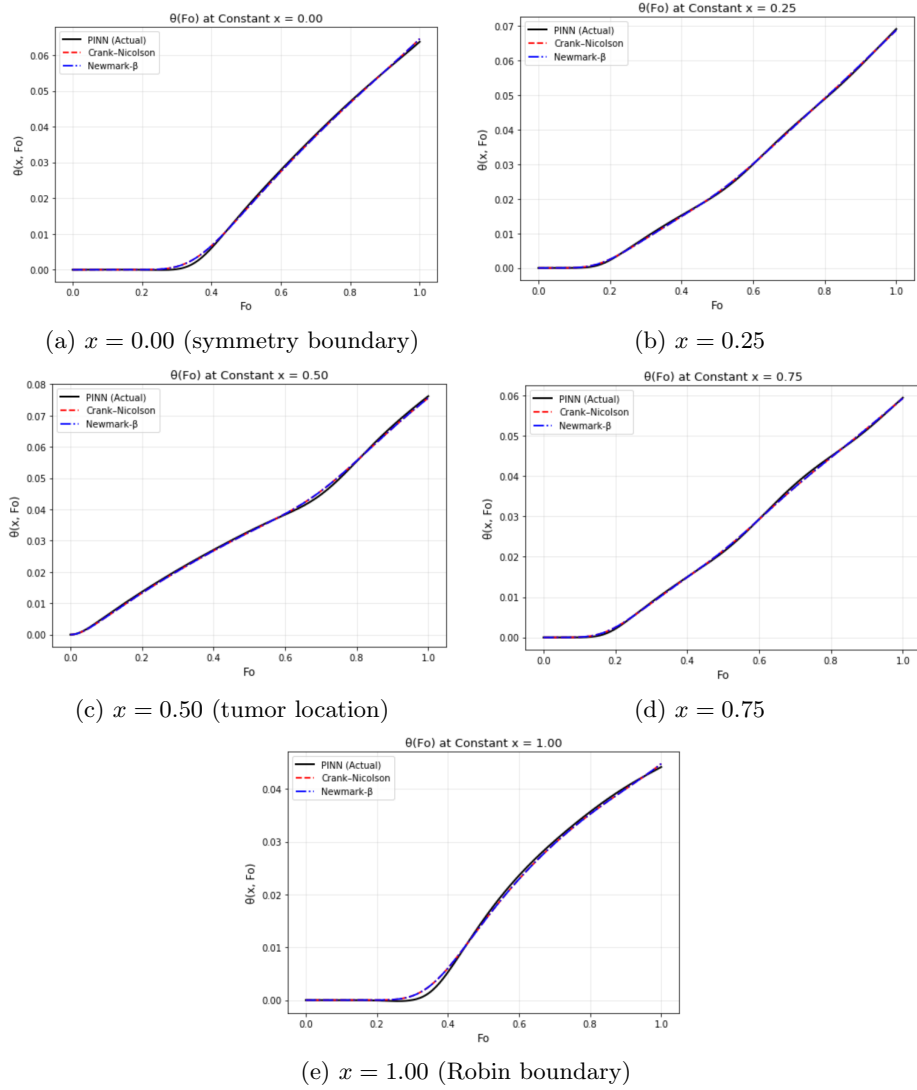


Figure 7: Temporal temperature evolution $\theta(F_o)$ at various spatial locations. The highest temperature rise occurs at the tumor center ($x = 0.5$), while boundary locations show slower heating rates.

- PINN results show excellent agreement with classical methods, with minor deviations visible only during rapid transitions (e.g., $x = 0.00$ at $F_o \approx 0.3$).

These line-by-line comparisons provide strong quantitative validation of the PINN approach. The nearly perfect overlay of all three curves across multiple spatial and temporal slices demonstrates that PINN successfully learns the underlying physics and produces results consistent with well-established numerical schemes.

While all three methods produce comparable results, each has distinct advantages:

- **Crank-Nicolson:** Computationally efficient for uniform grids, requires solving a sparse linear system at each time step.
- **Newmark- β :** Excellent for wave propagation problems, provides superior energy conservation.
- **PINN:** Mesh-free, provides continuous solution, flexible for complex geometries, but requires careful hyperparameter tuning and longer training time.

Conclusion

The PINN approach provides a viable and accurate method for solving the complex DPL bio-heat transfer equation, offering a robust alternative to the FEWGM. The results confirm the effectiveness of the **Gaussian heat source** in localizing the maximum temperature at the tumor site, which is critical for the success of hyperthermia treatment.

Validation against the Crank-Nicolson and Newmark- β schemes demonstrates that the PINN solution achieves comparable accuracy to classical finite difference methods while offering the additional advantage of a continuous, mesh-free representation of the solution. This makes PINN particularly attractive for future extensions to complex geometries, inverse problems, and real-time parameter estimation in clinical hyperthermia applications.